The *Hinode* X-Ray Telescope (XRT): Camera Design, Performance and Operations.

R. Kano[1], T. Sakao[2], H. Hara[1], S. Tsuneta[1], K. Matsuzaki[2], K. Kumagai[1], M. Shimojo[3], K. Minesugi[2], K. Shibasaki[3], E. E. DeLuca[4], L. Golub[4], J. Bookbinder[4], D. Caldwell[4], P. Cheimets[4], J. Cirtain[4], E. Dennis[4], T. Kent[4], M. Weber[4]

[1] *National Astronomical Observatory of Japan, 2-21-1 Osawa, Mitaka, Tokyo 181-8588, JAPAN* (ryouhei.kano@nao.ac.jp)

[2] *Institute of Space and Astronautical Science, Japan Aerospace Exploration Agency, 3-1-1 Yoshinodai, Sagamihara, Kanagawa 229-8510, JAPAN*

[3] *Nobeyama Solar Radio Observatory, National Astronomical Observatory of Japan, Nobeyama, Nagano 384-1305, JAPAN*

[4] *Smithsonian Astrophysical Observatory, 60 Garden Street, Cambridge, MA 02138, U.S.A.*

Received 15 June 2007; accepted 18 September 2007

Abstract. The X-ray Telescope (XRT) aboard the *Hinode* satellite is a grazing incidence X-ray imager equipped with a 2k×2k CCD. XRT has 1 arcsec pixels with wide field of view of 34×34 arcmin. It is sensitive to plasmas with wide temperature range from < 1 MK to 30 MK, allowing us to obtain TRACE-like low temperature images as well as Yohkoh/SXT-like high temperature images. Spacecraft mission data processor (MDP) controls XRT through sequence tables with versatile autonomous functions such as exposure control, region-of-interest tracking, flare detection and flare location identification. Data are compressed either with DPCM or JPEG, depending on the purpose. This results in higher cadence and/or wider field of view for a given telemetry bandwidth. With focus adjust mechanism, higher resolution of Gaussian focus may be available on-axis. This paper follows the first instrument paper for XRT (Golub *et al.*, 2007), and discusses the design and measured performance of the X-ray CCD camera for XRT, and its control system with MDP.

Keywords: Sun: corona, Sun: X-rays

1. Introduction

The Solar-B satellite was launched at 06:36 on September 23, 2006 (Japan Standard Time), and then named *"Hinode"* (Kosugi *et al.*, 2007). The X-Ray Telescope (XRT) aboard *Hinode* is a grazing incidence telescope designed to observe all the coronal features across a range of temperature not available to normal incidence telescopes. Golub *et al.* (2007) describes the XRT scientific objectives and requirements, and the design and performance of the telescope portion of XRT. This companion paper describes the X-ray camera.

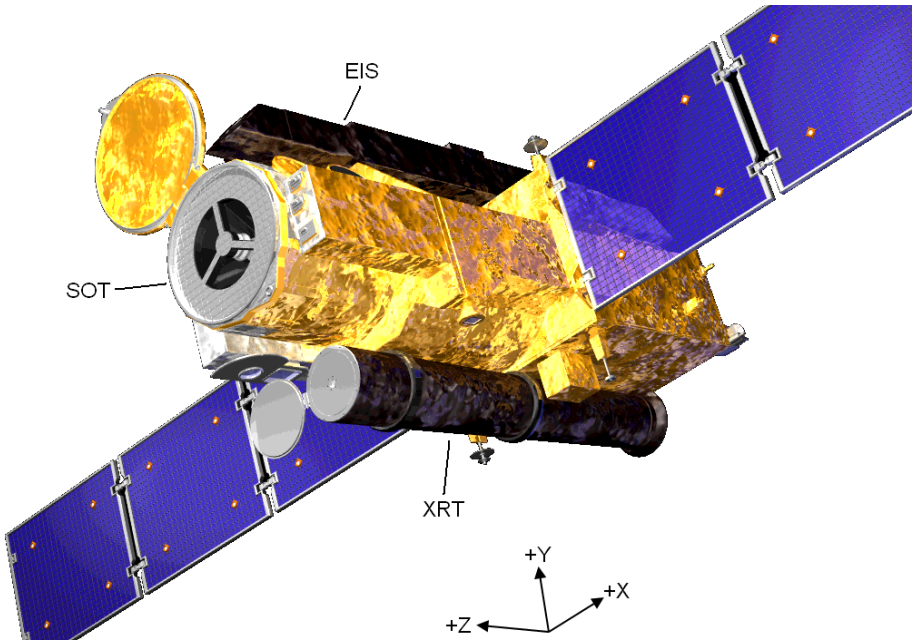

Figure 1. The *Hinode* satellite. XRT is located on the −Y side of the satellite body.

The XRT has the broadest temperature coverage of any coronal imager to date and an unprecedented combination of spatial resolution and field of view (Golub *et al.*, 2007). In the conceptual design phase of the strawman Solar-B mission around 1994–1996, there was an intense discussion on whether we should choose a grazing incidence optics or a normal incidence optics. The normal incidence optics can bring better spatial resolution, while the grazing incidence telescope is essentially sensitive to all temperatures. A dominant factor leading to the decision was the wide temperature range that the grazing incidence optics brings us. A great success of the TRACE mission undoubtedly shows the critical importance of high-resolution imaging (Golub *et al.*, 1999; Schrijver *et al.*, 1999). We, however, chose a balanced approach with regard to the conflicting scientific interests of spatial resolution, temperature range, and field of view. The choice resulted in apparent compromise in the spatial resolution with obvious advantage of the wider field of view. A large format 2k×2k CCD allows to cover the whole Sun, when the Sun is located at the center of the CCD. Note, however, that in nominal observing mode, *Hinode* tracks active regions or specific targets on the Sun that the other two telescopes aboard *Hinode* (the Solar Optical Telescope, SOT; Tsuneta *et al.*, 2007; Suematsu *et al.*, 2007; Ichimoto *et*

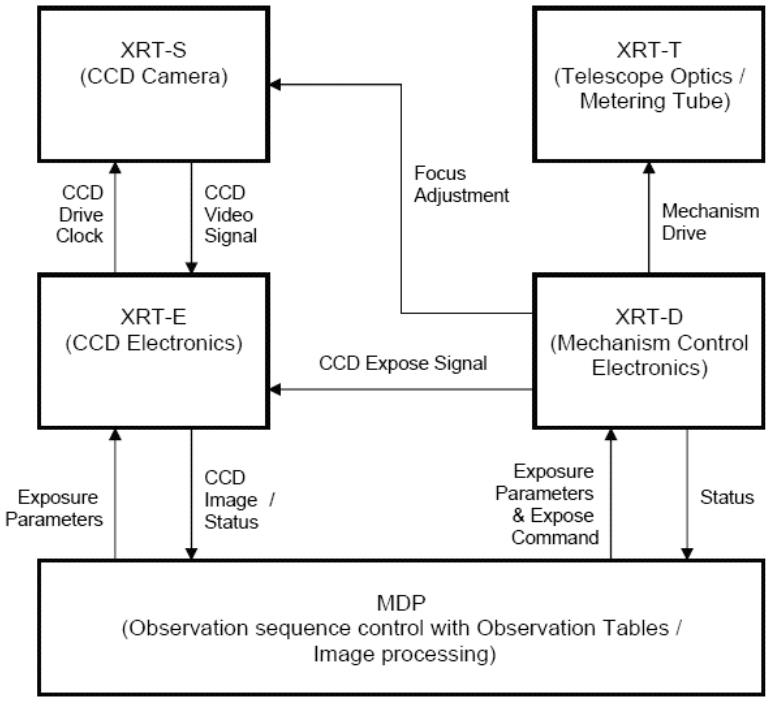

Figure 2. Block diagram showing four functional components of XRT together with MDP.

al., 2007; Shimizu *et al.*, 2007; Tarbell *et al.*, 2007 and the EUV Imaging Spectrometer, EIS; Culhane *et al.*, 2007) want to see, because they have a much smaller field of view as compared to XRT.

The spatial resolution of a telescope depends on the combination of focal length and pixel size (as well as quality of the mirror, of course). A longer focal length and a smaller pixel size make a higher spatial resolution. The lowest limit of the pixel size is, however, given by the requirement on the dynamic range of the image, because too small pixel size causes too small full-well capacity. The length of a grazing incidence telescope is almost identical with its focal length. Therefore, to improve the spatial resolution of the XRT, we designed a longer telescope. A heroic effort was made by the spacecraft design team: Namely, the whole spacecraft design was driven to make XRT (and EIS) as long as possible. Figure 1 of the *Hinode* outlook shows that XRT is as long as the entire length of the spacecraft. This results in the pixel size of one arcsec.

Figure 2 indicates four functional components constituting the XRT. XRT-T consists of the telescope metering tube including the X-ray and visible light optics and focal plane mechanisms (filter wheels, shutter and

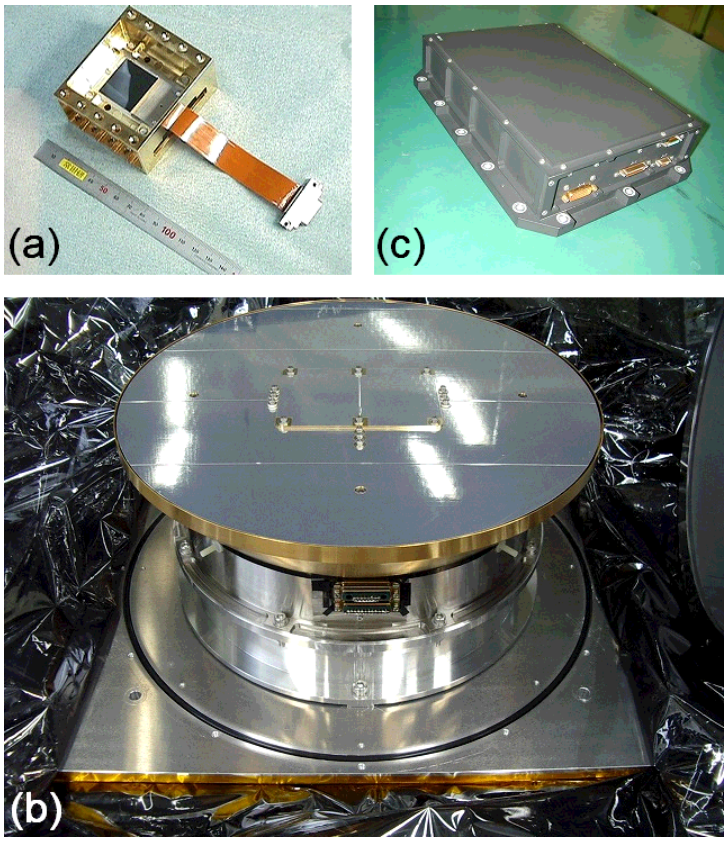

Figure 3. (a) XRT CCD installed in the CCD Invar housing (a mechanical sample). (b) XRT-S, the XRT camera, mounted on the base plate of its shipping container. (c) XRT-E, the camera electronics.

focus motor). XRT-D is the driving electronics for the focal plane mechanisms. XRT-S is the focal-plane CCD imager attached at the rear end of XRT-T. It includes a 2k×2k CCD device. XRT-E is the CCD electronics. The spacecraft Mission Data Processor (MDP) also plays a vital role for XRT. The *Hinode* XRT is the result of the Japan-US collaboration involving Smithsonian Astrophysical Observatory (SAO) with NASA MSFC (XRT-T and XRT-D), Institute of Space and Astronautical Science, Japan Aerospace Exploration Agency, and the National Astronomical Observatory of Japan (XRT-S, XRT-E and MDP). In Section 2, we discuss in detail the design, calibration and measured performance of the CCD camera (XRT-S and XRT-E, Figure 3). In Section 3 observation control of XRT with MDP, followed by brief description on the camera thermal performance in Section 4.

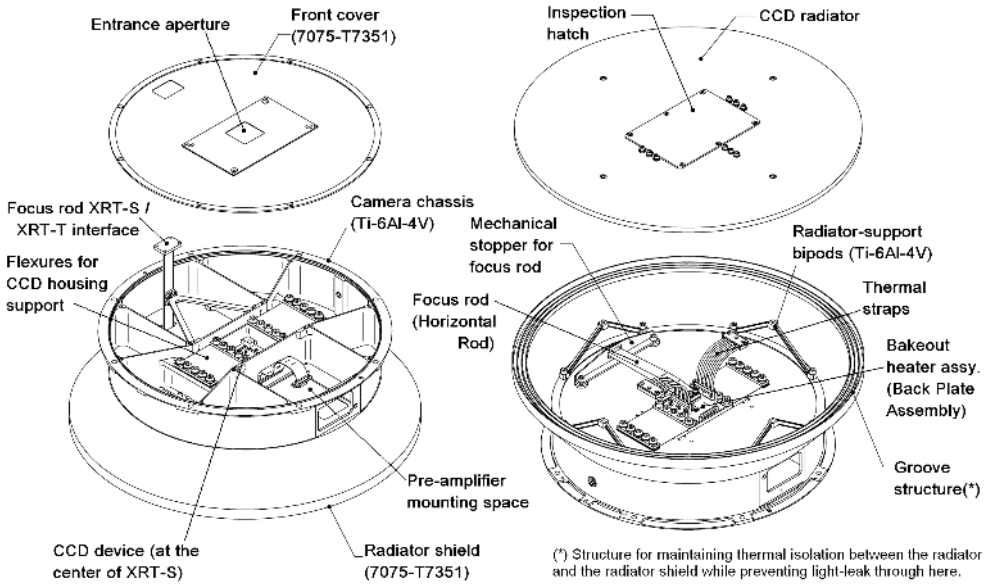

Figure 4. Schematic drawings of XRT-S. Left: Seen from the telescope side (Sun-facing side) with the front cover detached. Right: From the rear side (radiator side) with the radiator detached. Note the pre-amplifier, which is mounted inside XRT-S, is not shown in the figure.

2. Instruments

Grazing incidence optics has wide and continuous coverage in wavelengths. XRT utilizes a back-illuminated CCD to enhance the sensitivity of longer wavelengths as compared with Yohkoh/SXT (Tsuneta *et al.*, 1991) which was equipped with a front-illuminated CCD. This essentially makes XRT TRACE-like when we image the Sun with thin filters and SXT-like with thick filters as far as temperature sensitivity is concerned. What we will see with this telescope is mixture of them, depending on the differential emission measure within a pixel.

2.1. Camera Structure

XRT-S consists of a flat cylinder of the camera chassis and a skirt to the camera radiator (Figure 4). At the center of the chassis, the CCD housing is supported by two sets of thin flexures. This is a unique feature of XRT that

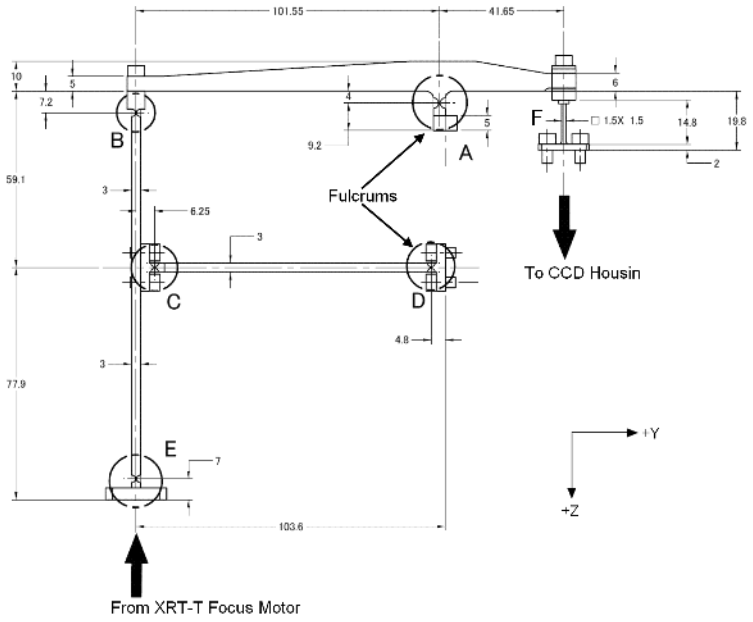

Figure 5. Focus mechanism rod system inside XRT-S. Portions shown by circles with labels A-E are elastic hinges. A and D are fixed to the XRT-S chassis, serving as fulcrums. The spacecraft coordinates are also shown.

provides a focus adjustment with a stroke of ±1mm along the optical axis by commands from the ground. This design was driven by consideration of risk mitigation, which significantly reduces the risk of defocus in orbit, which would otherwise be difficult to overcome given the size and the complexity of the X-ray telescope. In addition to the risk mitigation, the focus adjustment capability can be used in the scientific operation. Image plane of the grazing incidence optics is heavily curved as shown in Figure 3 of Golub *et al.* (2007). The focus adjustment allows us to choose either on-axis maximum resolution with rapid off-axis degradation (Gaussian focus, see the curve for 2700.00mm in the figure) or the focus position that gives resolution as uniform as possible over a larger field of view (Optimized focus, see the curve for 2699.77mm). Figure 5 shows the linkage structure of the focus rods in XRT-S. At the points A and D, the focus rods system is fixed to the chassis. Elastic hinges at A – E and an elastic pin at F give flexibility to the rods system. A push-pull motion from the focus motor mounted in XRT-T is transmitted to the portion F, and then the CCD housing is pushed/pulled from behind (−Z side).

The housing, which is made of Invar, is thermally isolated from the surrounding by the thin flexures and the gold plating on it, and connected to

Table I. XRT camera characteristics

CCD type	Back-illuminated three-phase CCD (e2v/CCD 42-40)
Pixel format	2048×2048 pixels
Pixel size	13.5×13.5 μm (corresponding to 1×1 arcsec)
Field of view	34×34 arcmin
Pixel binning mode	1×1, 2×2, 4×4 and 8×8
Dark current	0.1 e^-/s/pixel @ $-65°$C
CCD temperature	Passive cooling: $< -43°$C
CTE	Parallel > 0.999996,
	Serial > 0.999999 ($-93°\text{C} < T < -50°\text{C}$)
QE (X-ray/EUV)	0.93 @ 13Å, 0.61 @ 45Å, 0.46 @ 114Å, 0.56 @ 304Å
QE (visible light)	0.44 @ 4000 Å, 0.66 @ 5000 Å
Full-well capacity	2.0×10^5 e^-
Camera gain constant	57 e^-/DN
Camera system noise	< 30 e^-
Output data resolution	12 bit

the camera radiator with two flexible thermal straps (left of Figure 4). The radiator always points away from the sun, and is designed to keep the CCD housing and the CCD in it at a temperature below $-43°$C. The thermal capacities of the housing and the radiator reduce the orbital variation of the CCD temperature. The Invar housing also shields the CCD against high energy particles, to avoid degradation of the image quality.

Major components for XRT-S were extensively baked and outgases from them were measured with TQCMs during the assembly of XRT-S. For the outgas measurement, TQCM temperature was set to -84 – $-88°$C, because the coldest on-orbit (and also during pre-launch tests) predicted temperature for the CCD was $-78°$C, while the components were at room temperature. We set mass accumulation rate of 1.56×10^{-9} g cm^{-2} hr^{-1} onto the TQCM as a goal, which corresponds to accumulation thickness of 120Å/month in the case of material with $\rho \approx 1$ g cm^{-3}. While some components did not achieve the goal even after baking, we comfortably accepted them (mass accumulation rate 5×10^{-9} g cm^{-2} hr^{-1} in the worst case), because they were to be used outside of the camera. On the rear side of the CCD package, an on-orbit decontamination heater is attached. It will be turned on, to avoid the accumulation of outgases on the CCD in the initial phase, and to remove the accumulated outgases in the later phase.

2.2. CCD Performance

XRT uses a back-illuminated three-phase CCD with 13.5 μm pixel-size and 2048×2048 array, which was manufactured by e2v technologies. The CCD has two identical read-out ports; R-port and L-port. XRT uses R-port as the default port, and L-port as a backup. From either port, an entire CCD image can be read. Camera performance (camera gain, dark current, quantum efficiency, and CCD cooling) was calibrated in the Advanced Technology Center of the National Astronomical Observatory of Japan. Basic features of the camera, including some results from the calibration are briefly summarized in Table I. The camera system gain, the dark current, and the quantum efficiency are described in detail in the subsequent sections.

2.2.1. *Camera Gain*

The XRT camera gain was measured with an ^{55}Fe isotope at several CCD temperatures. Figure 6 (top) shows an example of the ^{55}Fe isotope data. Mn-Kα and Mn-Kβ lines are clearly seen. Figure 6 (bottom) summarizes measured camera gain for both readout ports over the CCD operation temperature from -43°C to -100°C. While there is a slight dependence on the CCD temperature as shown blow, we can reasonably adopt a value of 57 e$^-$/DN as the typical value for this temperature range. The fitted lines are,

$$G_{\rm R}[{\rm e}^-/{\rm DN}] \;=\; 59.1 + 0.026 \cdot T[^\circ{\rm C}], \tag{1}$$

$$G_{\rm L}[{\rm e}^-/{\rm DN}] \;=\; 58.8 + 0.034 \cdot T[^\circ{\rm C}]. \tag{2}$$

2.2.2. *Dark Current*

Figure 7 shows the temperature dependence of the dark current, and also shows three model curves calculated by the following general formula (Janesick, 2000);

$$D_{\rm R}[{\rm e}^-/{\rm s/pixel}] = 2.5 \times 10^{15}\ P_{\rm S}\ D_{\rm FM}\ T^{1.5}\ \exp(-E_{\rm g}/(2kT)), \tag{3}$$

where $P_{\rm S}$ is the pixel area (cm^2), $D_{\rm FM}$ is called the "dark current figure of merit" at 300K (nA cm^{-2}), T is the CCD temperature (K), k is Boltzmann's constant (8.62×10^{-5} eV K^{-1}), and $E_{\rm g}$ is the bandgap energy (eV) described by the following empirical formula

$$E_{\rm g}[{\rm eV}] = 1.1557 - \frac{7.021 \times 10^{-4} T^2}{1108 + T}. \tag{4}$$

Below -75°C, the dark current was too small to derive meaningful values with the longest-available exposure (64 s) with the test setup for the calibration. The remaining data points are well fitted to the model curve with $D_{\rm FM} = 0.4$ nA cm^{-2}. Because the CCD will be operated below -43°C on the

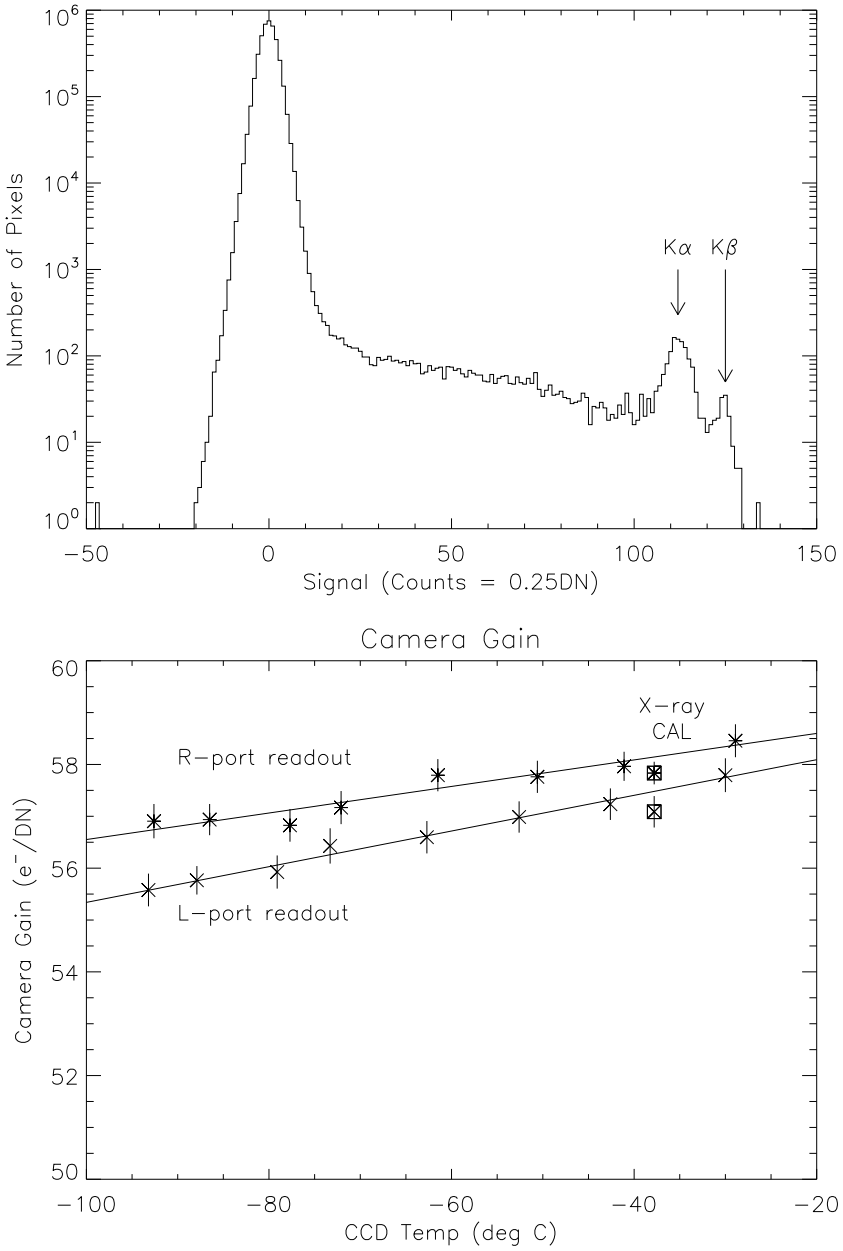

Figure 6. (Top) A histogram showing signal distribution for an ^{55}Fe image taken through R-port at -93°C, with dark current subtracted. Mn-Kα and Mn-Kβ lines are clearly seen around the signal values of 110 and 125, respectively. (Bottom) The system camera gain of the XRT camera taken during the thermal vacuum test (crosses). Error bars show 3σ statistical uncertainty. The data separately taken during the X-ray QE measurements is also shown by boxes.

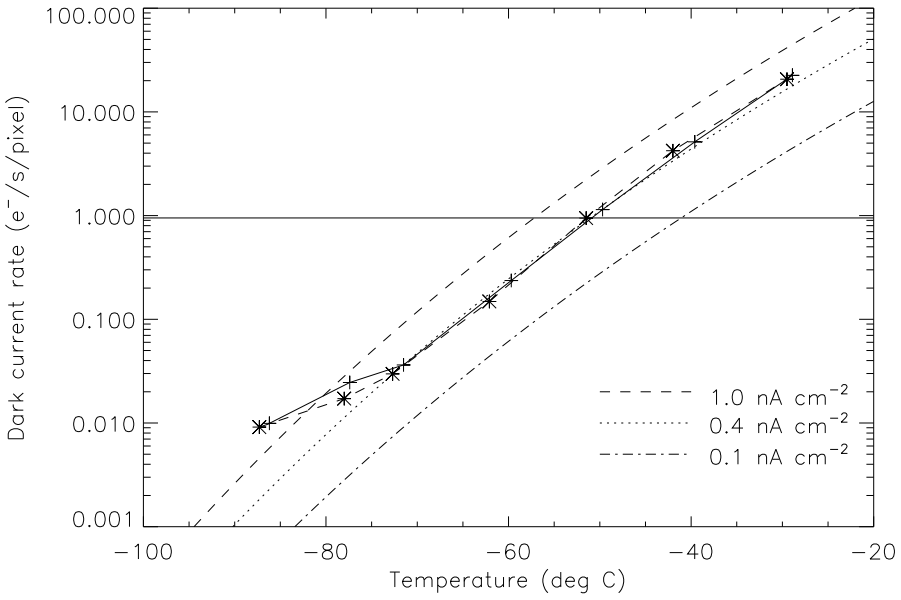

Figure 7. Temperature dependence of dark current for the XRT CCD. Crosses and stars show the data from R-port and L-port, respectively. The horizontal line shows a level of 1DN/64s. The dark current below −75°C is over estimated, and should not be regarded as real.

orbit, the dark current is at most a few DN even with the longest exposure for the camera (64 s).

2.2.3. *Quantum Efficiency*

The X-ray and EUV quantum efficiency was measured with 16 emission lines listed in Table II. From Mo-L 5.4Å to Be-K 114Å, we used the in-focus monochromator (IFM-SXR-0.5) manufactured by Hettrick Scientific, Inc. with the MANSON Model-2 X-ray Source of Austin Instruments, Inc. (Figure 8a). Above He-II 256Å, we used the EUV monochromator (LHT30) of Jobin-Yvon (Figure 8b). Figure 8 (c) and (d) show experiment configuration in the calibration chamber. A silicon photodiode manufactured by International Radiation Detectors (IRD) was used as the reference detector for the XRT CCD. The photodiode was calibrated by NIST (National Institute of Standards and Technology) in the wavelength range between 50 – 1200 Å. We also received the information on the thicknesses of the depletion layer and the oxide layer of this photodiode from the manufacturer, and extrapolated the photodiode QE with a simple model assuming silicon thickness of 25μm

Table II. Emission lines used for X-ray and EUV QE measurements

Line	Wavelength (Å)	Line	Wavelength (Å)	Line	Wavelength (Å)
Mn K	2.1*	Ni L	14.6	Be K	114
Mo L	5.4	Fe L	17.6*	He II	256
W K	7.0	O K	23.6	He II	304*
Al K	8.3*	Ti L	27.4	He I	584
Mg K	10.0*	C K	44.6*		
Cu L	13.3	Mo M	64.2		

* : L-port readout data was only taken at 6 wavelengths.

with 120Å top oxide layer, and the unity charge collection efficiency in the silicon. For Mn-K 2.1Å, we used an ^{55}Fe isotope whose X-ray count rate was calibrated by ourselves with the Manson Model 04 Gas Flow Proportional Counter.

Figure 9 shows the wavelength dependence of the quantum efficiency of the XRT CCD, with the best-fit QE curve. As shown in Stern *et al.* (1994), the charge collection efficiency (η) of back-illuminated CCD is low near the back surface. We adopted a simplified expression for this effect with an exponential function:

$$\eta(x) = 1 - (1 - \eta_0)\exp(-\gamma \cdot x), \tag{5}$$

instead of a linear function in Stern *et al.* (1994) of

$$\eta(x) = \begin{cases} \eta_0 + (1 - \eta_0) \cdot \gamma x & \text{for } 0 < x < \gamma^{-1} \\ 1 & \text{for } x > \gamma^{-1} \end{cases}, \tag{6}$$

to avoid somewhat clear boundary at the depth of γ^{-1} in the latter formula. In the above equations, η_0 is the charge collection efficiency at the back surface, γ is the inverse of the thickness of the back-surface effect, and x is the distance from the CCD back surface. Following Stern *et al.* (1994), we derive a model QE curve as

$$QE = e^{-\mu_{\rm SiO2} d_{\rm SiO2}} \int_0^{d_{\rm Si}} \eta(x) \cdot \mu_{\rm Si} \cdot e^{-\mu_{\rm Si} x} {\rm d}x, \tag{7}$$

$$= e^{-\mu_{\rm SiO2} d_{\rm SiO2}} \left\{ 1 - e^{-\mu_{\rm Si} d_{\rm Si}} - (1 - \eta_0) \frac{\mu_{\rm Si}}{\mu_{\rm Si} + \gamma} (1 - e^{-(\mu_{\rm Si} + \gamma) d_{\rm Si}}) \right\}, \tag{8}$$

where $d_{\rm Si}$ is the thickness of the silicon substrate, $d_{\rm SiO2}$ is the thickness of the oxidized layer on the back surface, and $\mu_{\rm Si}$ and $\mu_{\rm SiO2}$ are absorption coefficient of silicon and silicon dioxide. The best-fit curve shown in Figure

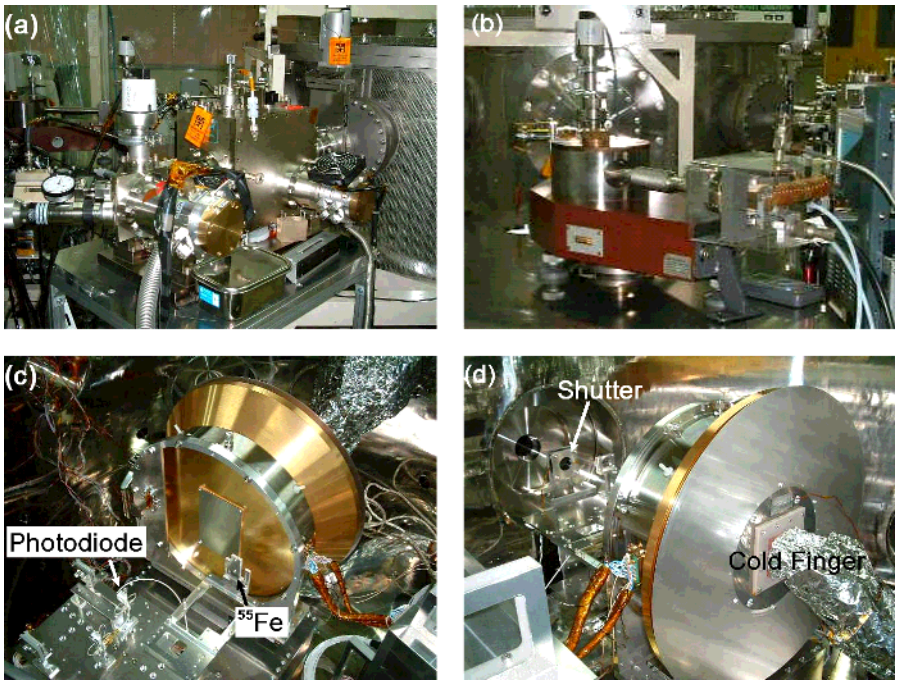

Figure 8. QE measurement configurations. Panels (a) and (b) show X-ray and EUV monochromators, respectively. Panels (c) and (d) show the setup in the calibration chamber with XRT-S. A reference photodiode, an ^{55}Fe isotope and a beam shutter were located in front of XRT-S. A cold finger was attached to the camera radiator from behind.

9 is calculated with parameters of $d_{\rm Si} = 14.4\mu$m, $d_{\rm SiO2} = 66$Å, $\eta_0 = 0.41$, and $\gamma = (0.21\mu{\rm m})^{-1}$.

3. Observation Control System

XRT is scientifically controlled by the spacecraft Mission Data Processor (MDP, see Figure 10). MDP has a capability to perform onboard processing of the XRT image data for autonomous observation control such as selection of regions of interest (Automatic Region Selector; ARS), Automatic Exposure Control (AEC), and Flare Detection (FLD). MDP also has dedicated pre-flare buffers within which series of pre-flare images can be stored. In this section, we describe the MDP functions for XRT observations from the viewpoint of an observer preparing his/her proposed observations.

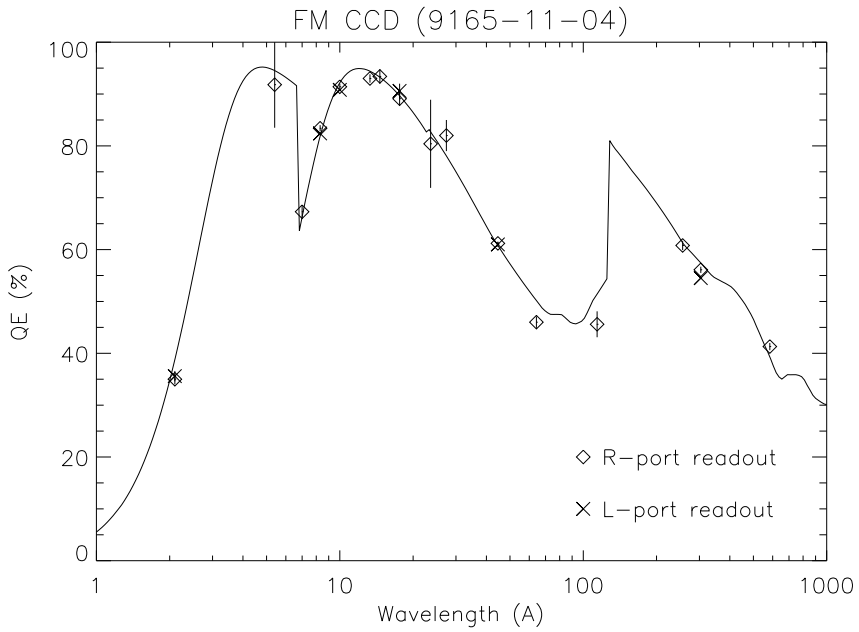

Figure 9. The quantum efficiency of the XRT CCD. Error bars shows 1σ statistical uncertainty. Solid curve indicates the best-fit QE curve from a CCD model described in the text.

3.1. Observation Tables

MDP controls XRT based on the observation tables stored inside MDP. The observation tables consist of three hierarchies of tables; main programs, subroutines and sequence tables.

Each sequence table includes a maximum of eight exposure commands, and is prepared as an elemental set of the XRT observations. For example, one sequence table may be designed for the full-disk temperature analysis with two alternate filters, and another for the DEM analysis with eight different filters in succession.

The sequence tables are building blocks for the main programs and subroutines. The observer can prepare the main programs and subroutines by combining the existing or newly prepared sequence tables for his/her proposed observations. The observer can also prepare a different main program for flare observations that is activated when the flare flag is set by the Flare Detection logic.

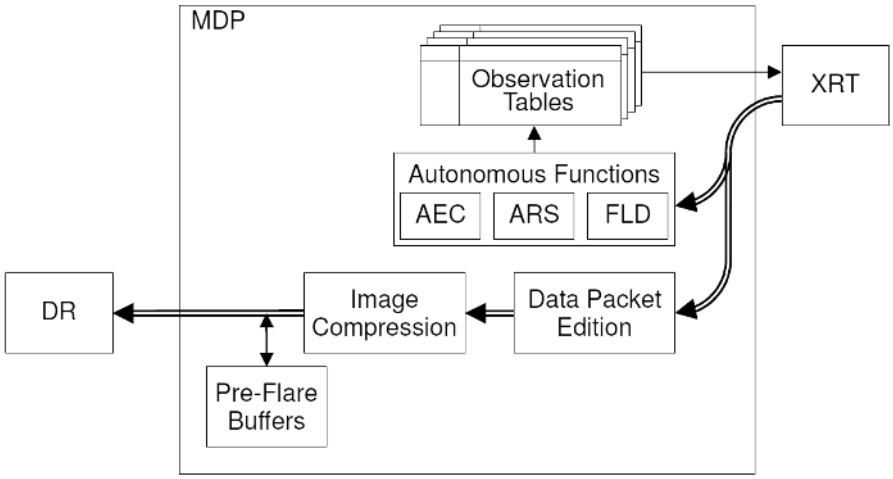

Figure 10. Functional block diagram of MDP for XRT observations. Arrows with double lines show the flow of image data. All the XRT images pass through data packet edition and image compression, and are stored in the data recorder (DR). Some of the images are also transferred to the functional blocks for autonomous functions where they are analyzed to update the observation parameters in the MDP.

3.2. Region-of-Interest (ROI) Management

XRT can take partial frame images. The horizontal and vertical size of the partial frame images are 64, 128, 192, 256, 384, 512, 768, 1024, 1536 and 2048 pixels. The observer can select either square or rectangular-shaped partial frame images (*e.g.* 1024×256, 256×512). The smallest size, 64 pixels is only available in a square image format. If the spacecraft is pointed to the center of the solar disk, the largest field of view (2048×2048 pixel = 34×34 arcmin) can cover the full solar disk.

In the MDP, up to 16 region-of-interests (ROIs) for observations can be managed with a table dedicated for them. Each ROI is specified by its location and size on the XRT CCD, and is given a unique ID number. Each exposure command refers to the ROI by its ID number in a sequence table. The observer can set the locations and sizes for the ROIs before their observation. Among 16 ROIs, the locations of ROI1 – ROI4 and the locations of ROI15 and ROI16 are dynamically updated by the ARS function and by the FLD function of the MDP, respectively (Table III), during the observation as described later. The sizes for ROIs are not updated by the MDP, and are kept to be the values set by the observer.

Table III. ROI table stored in the MDP

ROI No.	Purpose
1	The brightest region detected by the ARS global search.
2-4	Bright regions tracked by the ARS local search.
5-12	Static (not updated by MDP) ROIs set by the observer. (Note ROI5 is also used for the Pre-Flare function.)
15-16	Flares detected by the FLD function.

3.3. Automatic Exposure Control (AEC)

While X-ray luminosity of the corona ranges over eight orders of magnitude from coronal holes and outer corona to intense X-class flares, the CCD has a dynamic range of only three orders of magnitude. Often the coronal intensity changes rapidly when flares start. The correct exposure is realized by changing the exposure duration over a wide range. A set of available exposure durations is shown in Table IV. Table V shows the typical count rate for various coronal features through different filters. MDP analyzes X-ray images onboard right after each exposure, and adjusts their exposure duration in pipe-line manner. This function is called Automatic Exposure Control (AEC). (Note AEC is available for images whose size is smaller than or equal to 256 K pixels (*i.e.* 512×512 pixel image or 2048×128 pixel image).) If an X-ray image does not achieve the proper exposure with the shortest exposure, AEC automatically changes the X-ray analysis filter to a thicker filter pre-specified by the observer in sequence tables.

Note that AEC can be disabled for any exposure in observation tables. It is also possible to intentionally take over- or under-exposed images for any exposure by changing the AEC parameters. This is often quite useful as demonstrated by Yohkoh, for observing, *e.g.*, faint objects surrounding a bright structure.

3.4. Automatic Region Selector (ARS)

The Automatic Region Selector (ARS) is the function that is used to search for bright regions and to automatically change the coordinates of the partial frame images to observe the new region. For this purpose, XRT takes full frame CCD images with a 2 arcsec resolution (ARS patrol images) at a regular interval. The time resolution of ARS, *i.e.* update interval for the region selection, depends on the cadence of ARS patrol images that can be set in the table. The baseline of the ARS time resolution is about 1.5 hours.

There are global search and local search modes in ARS, which function independently of each other. The global search selects the brightest region

Table IV. Exposure table

Index : Exposure	Index : Exposure	Index : Exposure	Index : Exposure
0 : 1 ms	8 : 24 ms	16 : 354 ms	24 : 5.66 s
1 : 2 ms	9 : 32 ms	17 : 500 ms	25 : 8.00 s
2 : 3 ms	10 : 44 ms	18 : 707 ms	26 : 11.3 s
3 : 4 ms	11 : 63 ms	19 : 1.00 s	27 : 16.0 s
4 : 5 ms	12 : 86 ms	20 : 1.41 s	28 : 22.6 s
5 : 8 ms	13 : 125 ms	21 : 2.00 s	29 : 32.0 s
6 : 12 ms	14 : 177 ms	22 : 2.83 s	30 : 45.2 s
7 : 16 ms	15 : 250 ms	23 : 4.00 s	31 : 64.0 s

Table V. Typical count rate (unit : DN/pixel)

	Coronal hole		Quiet sun		Active region		Flare (M2)	
Exposure (s)	45.2	64.0	11.3	32.0	0.50	4.0	0.001	0.004
Thin-Al/Mesh	124	175	300	850	949	sat.	sat.	sat.
Thin-Al/Poly	16	23	139	394	894	sat.	sat.	sat.
C/Poly	3	5	74	209	544	sat.	sat.	sat.
Ti/Poly	3	5	57	161	386	sat.	sat.	sat.
Thin-Be	0	0	15	44	204	1632	sat.	sat.
Med-Be	0	0	2	5	27	219	1419	sat.
Med-Al	0	0	1	3	14	111	619	2477
Thick-Al	0	0	0	0	2	14	90	361
Thick-Be	0	0	0	0	0	0	6	23

References of the model DEMs: Data for "Coronal hole", "Quiet sun" and "Active region" adopted from Vernazza & Reeves (1978), and "Flare (M2)" from Dere & Cook (1979). If the count rate exceeds 3000DN, it is shown as "sat."

on the entire XRT CCD, and updates the location of ROI1 (see Table III). The local search tracks the brightest region in each of ROI2, 3 and 4, by searching a limited area around the current location. The locations and sizes for these ROIs are initially set by the observer, With the local search we can track up to three targets in parallel.

3.5. Flare Detection (FLD)

Hinode has no independent X-ray detection system dedicated to identify solar flares. Thus, XRT has to do this by itself using a Flare Detection (FLD) algorithm. FLD automatically identifies the occurrence of a flare,

then determines the flare location on the CCD, and finally sets a flare flag for the XRT as well as for the SOT and the EIS. For this purpose, XRT takes full frame CCD images with an 8 arcsec resolution (called FLD patrol images) at a regular interval. The baseline of FLD patrol interval is about 30 seconds.

The method to identify flares is not based on a simple intensity threshold monitoring of the FLD patrol images. Since many solar flares are generally not so bright at the beginning in soft X-rays, if flares are to be detected as soon as they occur, a simple threshold-based detection algorithm does not suffice. A better FLD algorithm is to monitor the increase in intensity by comparing with a running-averaged patrol image generated based on a collection of FLD patrol images taken previously. MDP calculates the parameter q^2 which is actually a map to represent increase of the X-ray intensity normalized by photon noise;

$$q^2(x,y) = \frac{(F(x,y) - F_{\rm avg}^{(i-1)}(x,y))^2}{F_{\rm avg}^{(i-1)}(x,y) + g} \qquad \text{for} \quad F > F_{\rm avg}^{(i-1)}, \tag{9}$$

where g is a control parameter to avoid division by 0, F is the patrol image to be evaluated, and $F_{\rm avg}^{(i)}$ is the running-averaged patrol image calculated by

$$F_{\rm avg}^{(i)}(x,y) = \gamma F(x,y) + (1-\gamma) F_{\rm avg}^{(i-1)}(x,y). \tag{10}$$

γ is also a parameter which controls the effective duration of the running average. If q^2 exceeds a threshold for flare start, MDP sets the flare flag and finds a flare location in F-map around the peak location in q^2-map. The flare location will be dynamically set as the center position of ROI15 and ROI16, which are then referred to from sequence tables. The observer can set the sizes of ROI15 and ROI16 before observations. When q^2 becomes lower than a threshold for flare end, MDP drops the flare flag.

FLD also has a capability of the detection of radiation belts. In radiation belts, MDP changes the parameters of the flare detection algorithm to avoid spurious effects of charged particles in identifying flare occurrence.

3.6. Image Compression

The CCD video signal is digitized with a 14-bit analog-to-digital converter in the XRT-E, the upper 12 bit of which is then sent to MDP. The observer can specify three types of compression for each exposures in sequence tables; no compression, lossless compression and lossy compression. In the no-compression mode, MDP is transparent. In the lossless compression, MDP compresses images with the differential pulse code modulation (DPCM) method which does not lose any information of the image. The efficiency of DPCM for XRT images is expected to be about 50% (*i.e.* 6 bit/pixel)

Table VI. Time cadences for three typical examples

Example 1	Continuous observation of an active region
ROI	FOV=384×384 arcsec, Binning=1×1 arcsec
Time interval of a pair of filter images	
	30 s
Data rate	576 k pixel min^{-1}
Example 2	High-speed observation of an active region
ROI	FOV=384×384 arcsec, Binning=1×1 arcsec
Time interval of a pair of filter images	
	5 s
Period	10 minutes observation and 50 minutes intermission
Data rate	576 k pixel min^{-1}
Example 3	Combination of full frame and partial frame images
ROI1	FOV=384×384 arcsec, Binning=1×1 arcsec
ROI2	FOV=2048×2048 arcsec, Binning=4×4 arcsec
Time interval of a pair of filter images	
	ROI1 = 40 s and ROI2 = 200 s
Data rate	586 k pixel min^{-1}

according to simulation studies. This is a popular option to reduce the amount of telemetry data. In the lossy compression, MDP compresses images with JPEG method whose quality factor can be specified for each exposure when preparing observation tables depending on the purpose. The JPEG compression may be useful for providing context images for SOT and EIS or for performing purely morphological studies.

3.7. Exposure Cadence

The time cadence for a series of exposures depends on the following pre and post-exposure activities: (1) Set-up time for the focal plane mechanisms, especially the filter wheel movements: A movement to an adjacent filter position takes about 0.8 s. (2) Read-out time of the CCD image: It takes 9.3 s to read out a full-frame CCD image. (3) Image processing time in MDP: The autonomous functions in MDP can catch up the exposure cadence as fast as 2 s interval. (4) Restriction of the allocated data rate as described later. If the observer plans to take images at a high rate, the number of filters and/or the image size may have to be adjusted to keep within the data rate allocated for XRT.

Table VII. An example of pre-flare observation

ROI	FOV=384×384 arcsec, Binning=1×1 arcsec
Time interval of a pair of filter images	
Before $X - 160$ s	40 s ("X" is the on-set time of a flare.)
$X - 160$ s – $X - 100$ s	20 s
$X - 100$ s – X	10 s

The total data rate of the *Hinode* satellite depends on the frequency of the data recorder playback through downlink stations. A typical frequency of playback is about 15 downlinks/day. The total data rate is estimated to be 400 kbps for the scientific instruments. SOT, XRT and EIS are typically allocated 70%, 15% and 15% of the bandwidth, respectively. XRT image data is 12 bit/pixel and would be compressed to about 6 bit/pixel by DPCM. Therefore, the typical data rate for XRT is about 600 k pixel min^{-1}.

Following three examples are shown in Table VI. (1) For a continuous observation of an active region, a pair of two filter images is taken every 30 seconds. (2) For a fast cadence observation of an active region, a pair of two filter images is taken every 5 seconds. Such burst observation is available for a limited time interval to keep the averaged rate at about 600 k pixel min^{-1}. (3) For a combination of observations of an active region and its surrounding region, a pair of two filter images covering an active region is taken every 40 seconds, while the same pair of images covering the entire CCD is taken every 200 seconds.

3.8. Pre-Flare Buffers

In the MDP, four memory buffers are prepared for XRT images. One of them is used for the normal image transfer. The other three are used as ring buffers dedicated for pre-flare images. The observer can select the use of these special buffers for pre-flare observations. Once MDP detects the occurrence of a flare and if the flare occurs within the field of view of ROI5, MDP protects the data in the pre-flare buffers from being overwritten until the data is downlinked or the protection is released by a command. If MDP does not detect a flare in ROI5, MDP keeps overwriting the previous data in the pre-flare buffers. Because ROI5 is used in the logic to freeze the pre-flare buffers, it is recommended to use ROI5 for pre-flare observations. The size of the pre-flare buffers is 5.5 Mbytes in total. The observer can compose a wide variety of pre-flare observation using these pre-flare buffers. Table VII shows an example for the pre-flare observation that takes an active region image with a pair of X-ray analysis filters for the temperature diagnostics.

4. Thermal Performance of the CCD Camera

Just after the launch, the decontamination heater for the CCD was turned on to avoid accumulation of outgas onto the CCD. During this CCD bakeout period, the heater had kept CCD at about 30°C, while its surroundings kept at 10°C. The radiator temperature was −40°C. One month later, the heater was turned off, and the radiator and CCD were cooled down to −75°C and −69°C, respectively. The orbital variation of the CCD temperature is smaller than ±1°C during the non-eclipsing period.

5. Conclusion

The initial observations of the XRT have already begun. The on-orbit performance of the XRT camera is excellent and has met or exceeded all pre-launch expectations. The XRT is proving to be a powerful tool for investigating the many forms of coronal activity and is expected to reveal, though coordinated observations with the *Hinode* Solar Optical Telescope and EUV Imaging Spectrometer, the mechanisms of coronal heating.

Acknowledgements

We would like to thank our scientific and engineering colleagues of XRT at the Smithsonian Astrophysical Observatory (SAO), the National Astronomical Observatory of Japan (NAOJ), and the Institute of Space and Astronautical Science of JAXA (ISAS/JAXA). We also would like to thank Kenji Hiyoshi, Michihiro Horii and Koji Taguchi of Meisei Electric Co., Ltd. for developing the XRT camera electronics, Satoru Iwamura, Zhangong Du and Mitsuhiko Nakano of Astro Research Corp. for developing the XRT camera structures and thermal design, Peter Pool and Wolfgang Suske of e2v technologies (UK) ltd. and Kiyoshi Tabata of Cornes Dodwell Ltd. for providing the best quality CCD suited to XRT, Masahiro Koyama of Mitsubishi Heavy Industries, Ltd. for developing the MDP hardware, Katsuya Yamamoto and Masayuki Nagase of Systems Engineering Consultants Co., Ltd. for developing the MDP software, Tomonori Tamura of NAOJ for supporting the baking and outgas measurements of XRT-S, Tetsuo Nishino and Norio Okada of the Advanced Technology Center (ATC) of NAOJ for developing equipments for the XRT-S calibrations, Akira Ohnishi of ISAS/JAXA for advising the thermal design of XRT-S, and Kazuyuki Hirose of ISAS/JAXA for advising the electric design of XRT-S and XRT-E. We would like to thank the National Astronomical Observatory of Japan for financial support for developing the calibration facility in the ATC for the XRT CCD camera system.

We wish to express our sincere gratitude to late Prof. Takeo Kosugi, former project manager of *Hinode* at ISAS, who passed away suddenly in November 2006. Without his leadership in the development of Solar-B/*Hinode*, this mission would have never been realized.

Finally, we would like to thank Roger Hauck of SAO for developing the electrical interface between XRT-D and XRT-E with us. Unfortunately, he passed away before the launch of *Hinode*. We hope his soul rests in peace.

References

Culhane, J. L., Harra, L. K, James, A. M., Al-Janabi, K., Bradley, L. J., Chaudry, R. A., *et al.*: 2007, *Solar Phys.*, in press.

Dere, K. P. and Cook, J. W.: 1979, *Astrophys. J.* **229**, 772.

Golub, L., Bookbinder, J., DeLuca, E., Karovska, M., Warren, H., Schrijver, C. J., *et al.*: 1999, *Phys. Plasmas* **6**, 2205.

Golub, L., DeLuca, E., Austin, G., Bookbinder, J., Caldwell, D., Cheimets, P., *et al.*: 2007, *Solar Phys.*, in press.

Ichimoto, K., Lites, B., Elmore, D., Suematsu, Y., Tsunete, S., Katsukawa, Y., *et al.*: 2007, *Solar Phys.*, submitted.

Janesick, J. R.: 2000, *Scientific Charge-Coupled Devices*, SPIE Press.

Kosugi, T., Matsuzaki, K., Sakao, T., Shimizu, T., Sone, Y., Tachikawa, S., *et al.*: 2007, *Solar Phys.*, in press.

Schrijver, C. J., Title, A. M., Berger, T. E., Fletcher, L., Hurlburt, N. E., Nightingale, R. W., *et al.*: 1999, *Solar Phys.* **187**, 261.

Shimizu, T., Nagata, S., Tsuneta, S., Tarbell, T., Edwards, C., Shine, R., *et al.*: 2007, *Solar Phys.*, submitted.

Stern, R. A., Shing, L. and Blouke, M. M.: 1994, *Appl. Opt.* **33**, 2521

Suematsu, Y., Tsuneta, S., Ichimoto, K., Shimizu, T., Otsubo, M., Katsukawa, Y., *et al.*: 2007, *Solar Phys.*, submitted.

Tarbell, T. D., *et al.*: 2007, *Solar Phys.*, submitted.

Tsuneta, S., Acton, L., Bruner, M., Lemen, J., Brown, W., Caravalho, R., *et al.*: 1991, *Solar Phys.* **136**, 37.

Tsuneta, S., Suematsu, Y., Ichimoto, K., Shimizu, T., Otsubo, M., Nagata, S., *et al.*: 2007, *Solar Phys.*, submitted.

Vernazza, J. E. and Reeves, E. M.: 1978, *Astrophys. J. Suppl.* **37**, 485.